

# On the consistent choice of effective permittivity and conductivity for modeling graphene

YOUNGJOON HONG<sup>1</sup> AND DAVID P. NICHOLLS<sup>2,\*</sup> 

<sup>1</sup>Department of Mathematics, Sungkyunkwan University, Suwon 440-746, Republic of Korea

<sup>2</sup>Department of Mathematics, Statistics, and Computer Science, University of Illinois at Chicago, Chicago, Illinois 60607, USA

\*Corresponding author: davidn@uic.edu

Received 28 April 2021; revised 16 August 2021; accepted 19 August 2021; posted 20 August 2021 (Doc. ID 430088); published 23 September 2021

Graphene has transformed the fields of plasmonics and photonics, and become an indispensable component for devices operating in the terahertz to mid-infrared range. Here, for instance, graphene surface plasmons can be excited, and their extreme interfacial confinement makes them vastly effective for sensing and detection. The rapid, robust, and accurate numerical simulation of optical devices featuring graphene is of paramount importance and many groups appeal to Black-Box Finite Element solvers. While accurate, these are quite computationally expensive for problems with simplifying geometrical features such as multiple homogeneous layers, which can be recast in terms of interfacial (rather than volumetric) unknowns. In either case, an important modeling consideration is whether to treat the graphene as a material of small (but non-zero) thickness with an effective permittivity, or as a vanishingly thin sheet of current with an effective conductivity. In this contribution we ponder the correct relationship between the effective conductivity and permittivity of graphene, and propose a new relation which is based upon a concrete mathematical calculation that appears to be missing in the literature. We then test our new model both in the case in which the interface deformation is non-trivial, and when there are two layers of graphene with non-flat interfacial deformation. © 2021 Optical Society of America

<https://doi.org/10.1364/JOSAA.430088>

## 1. INTRODUCTION

Graphene, a sheet of carbon atoms in a honeycomb lattice, has transformed the fields of plasmonics and photonics with its blend of remarkable mechanical, chemical, and electronic properties [1]. First isolated experimentally in 2004, resulting in the awarding of the 2010 Nobel Prize to Geim [2] and Novoselov [3], graphene has become indispensable for devices operating in the terahertz to mid-infrared range where graphene surface plasmons (GSPs) can be excited [4]. The extreme interfacial confinement of these GSPs renders them vastly effective for sensing and detection. Recent work on graphene and other two-dimensional materials can be found in [5–8] while survey articles [9–13] describe the use of graphene in engineering devices.

From these considerations, it is clear that the rapid, robust, and accurate numerical simulation of optical devices featuring graphene is of paramount importance. Most engineering groups appeal to Black-Box Finite Element solvers such as COMSOL Multiphysics [14], e.g., [8,15], and a general overview of numerical methods for plasmonics problems can be found in the survey paper of Gallinet *et al.* [16]. While such simulations provide accurate solutions, they are typically exceedingly computationally expensive for problems with simplifying geometrical features. For instance, diffraction grating structures

with multiple homogeneous layers can be modeled with systems of differential equations featuring *interfacial* (rather than *volumetric*) unknowns, see, e.g., [17]. It was recently shown how such formulations can be extended to the case where two-dimensional materials are present [18,19] and these materials are modeled as *vanishingly thin* sheets of current with an effective conductivity. This approach has been adopted by several other groups, and we point to the surveys [20,21] and the recent work of [11,22–25].

However, an alternative approach which fits much more naturally into the framework of standard FEMs is to model the graphene as a thin layer of *finite* (but small) thickness with an effective permittivity. The question we entertain in this contribution is the correct relationship between the (non-dimensionalized) effective conductivity,  $\hat{\sigma}^{(g)}$ , and effective permittivity,  $\epsilon^{(g)}$ , of graphene. The relationship given in [11,22] is

$$\hat{\sigma}^{(g)} = \frac{k_0 d_g \epsilon^{(g)}}{i}, \quad (1)$$

where  $d_g$  is the graphene layer thickness (reported in [11,22] as 0.34 nm) and  $k_0 = \omega/c_0$  is the free-space wavenumber. In this paper, we propose a new relation

$$\hat{\sigma}^{(g)} = \frac{k_0 d_g E(h)}{i}, \quad (2)$$

where  $E(h)$  is given in Eq. (10),

$$\lim_{h \rightarrow 0} E(h) = E_0 := \epsilon^{(g)} + \frac{\sqrt{\epsilon^{(w)}}}{2} \left( \sqrt{\epsilon^{(u)}} - \sqrt{\epsilon^{(w)}} \right),$$

$h = d_g/2$ , and  $\epsilon^{(u)}$  and  $\epsilon^{(w)}$  are permittivities of the mounting structure above and below, respectively, the graphene sheet. As we shall show, this is based upon a concrete *mathematical* calculation which appears to be missing in the literature. For this, we make several simplifying assumptions to make progress with our rather *explicit* calculations. More specifically, we match these two approaches in the case of normal incidence and a flat interface between the dielectrics which mount the graphene sheet. We then test our results more fully in the case where the interface deformation is non-trivial in order to assess the utility of our formula for the effective conductivity. Such a comparison is of vital importance, as corrugated gratings are one of the principal mechanisms for generating graphene surface plasmons (GSPs) [21,26].

The organization of the paper is as follows: In Section 2, we recall the governing equations, first for a triply layered medium in Section 2.A and then for a doubly layered medium with an interfacial current in Section 2.B. In Section 3, we derive a more faithful formula for the effective conductivity in terms of the permittivity of graphene, while in Section 3.A we report a standard Drude model for this permittivity. In Section 4, we discuss the outcomes of our numerical simulations, with a description of our numerical methods in Section 4.A and a full commentary on figures which summarize our discoveries in Section 4.B, more specifically for a single graphene sheet in Section 4.C and a double sheet configuration in Section 4.D.

## 2. GOVERNING EQUATIONS

We consider the simplest possible configurations to connect the effective permittivity of graphene and its effective conductivity: A triply layered medium and a doubly layered structure with an interfacial current (see Fig. 1).

We begin with the case of flat interfaces, but later in the paper we will test the integrity of our calculations by considering the same structures with periodically *corrugated* interfaces. We now discuss each of these two models.

### A. Triply Layered Medium

For the triply layered configuration, we consider  $y$ -invariant, periodically corrugated interfaces at  $z = h + g(x)$ ,  $g(x + d) = g(x)$ , and  $z = -h + \ell(x)$ ,  $\ell(x + d) = \ell(x)$ . These determine three domains,

$$S^{(u)} = \{z > h + g(x)\}, \quad S^{(w)} = \{z < -h + \ell(x)\},$$

$$S^{(v)} = \{-h + \ell(x) < z < h + g(x)\},$$

filled with materials of permittivities  $\{\epsilon^{(u)}, \epsilon^{(v)}, \epsilon^{(w)}\}$ . The structure is illuminated by transversely polarized, monochromatic, plane-wave incidence of frequency  $\omega$  and wavenumber  $k^{(u)} = \sqrt{\epsilon^{(u)}} k_0$ ,

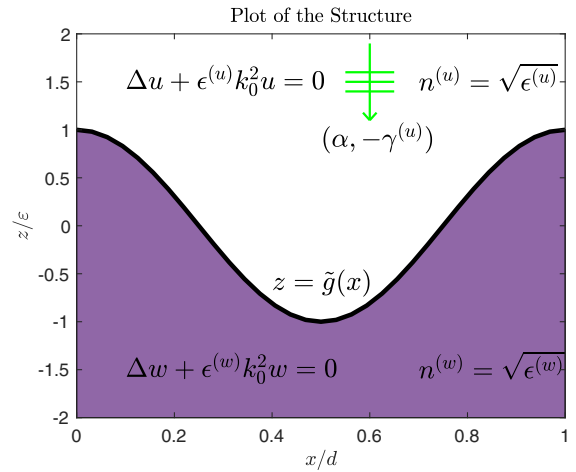


**Fig. 1.** Plot of the structure under consideration: graphene mounted on dielectric under vacuum. Structure rescaled by the period in the  $x$  coordinate and the maximum amplitude in the  $z$  coordinate.

$$u^{\text{inc}}(x, z) = e^{i\alpha x - i\gamma^{(u)} z}, \quad \alpha = k^{(u)} \sin(\theta), \quad \gamma^{(u)} = k^{(u)} \cos(\theta).$$

It is not difficult to see that the governing equations for the scattered transverse components of the fields in each layer,  $\{u, v, w\}$ , are [27]

$$\Delta u + \epsilon^{(u)} k_0^2 u = 0, \quad \text{in } S^{(u)}, \quad (3a)$$

$$\Delta v + \epsilon^{(v)} k_0^2 v = 0, \quad \text{in } S^{(v)}, \quad (3b)$$

$$\Delta w + \epsilon^{(w)} k_0^2 w = 0, \quad \text{in } S^{(w)}, \quad (3c)$$

$$u - v = \xi, \quad z = h + g(x), \quad (3d)$$

$$\tau^{(u)} \partial_N u - \tau^{(v)} \partial_N v = \tau^{(u)} v, \quad z = h + g(x), \quad (3e)$$

$$v - w = 0, \quad z = -h + \ell(x), \quad (3f)$$

$$\tau^{(v)} \partial_N v - \tau^{(w)} \partial_N w = 0, \quad z = -h + \ell(x). \quad (3g)$$

In these,  $\partial_N$  denotes the normal derivative  $\partial_N = N \cdot \nabla$  and

$$\tau^{(m)} = \begin{cases} 1, & \text{Transverse Electric (TE),} \\ 1/\epsilon^{(m)}, & \text{Transverse Magnetic (TM),} \end{cases}$$

where  $m \in \{u, v, w\}$ . It is understood that solutions are quasiperiodic, and that  $u$  and  $w$  are upward and downward propagating, respectively.

We now focus on the case of *flat* interfaces and normal incidence ( $\theta = 0$ ), and recall that the Rayleigh expansions [27] give upward/downward propagating quasiperiodic solutions to this problem of the form

$$u = \sum_{p=-\infty}^{\infty} a_p e^{i\alpha_p x + i\gamma_p^{(u)}(z-h)}, \quad (4a)$$

$$w = \sum_{p=-\infty}^{\infty} d_p e^{i\alpha_p x - i\gamma_p^{(w)}(z+h)}, \quad (4b)$$

$$v = \sum_{p=-\infty}^{\infty} \left\{ b_p \frac{\sin(\gamma_p^{(v)}(h+z))}{\sin(2\gamma_p^{(v)}h)} + c_p \frac{\sin(\gamma_p^{(v)}(h-z))}{\sin(2\gamma_p^{(v)}h)} \right\} e^{i\alpha_p x}, \quad (4c)$$

where  $\alpha_p = \alpha + 2\pi p/d = 2\pi p/d$  and

$$\gamma_p^{(m)} = \sqrt{\epsilon^{(m)} k_0^2 - \alpha_p^2} = \sqrt{\epsilon^{(m)} k_0^2 - \left(\frac{2\pi p}{d}\right)^2}, \quad m \in \{u, v, w\}.$$

Now, Eqs. (3d)–(3g) imply

$$\begin{pmatrix} 1 & -1 & 0 & 0 \\ -G_p & -H_p & -K_p & 0 \\ 0 & 0 & 1 & -1 \\ 0 & -K_p & -H_p & -J_p \end{pmatrix} \begin{pmatrix} a_p \\ b_p \\ c_p \\ d_p \end{pmatrix} = \begin{pmatrix} \hat{\xi}_p \\ \tau^{(u)} \hat{v}_p \\ 0 \\ 0 \end{pmatrix},$$

where

$$G_p := -\tau^{(u)} i\gamma_p^{(u)}, \quad J_p := -\tau^{(w)} i\gamma_p^{(w)},$$

$$H_p := \tau^{(v)} \gamma_p^{(v)} \cot(\gamma_p^{(v)} 2h), \quad K_p := -\tau^{(v)} \gamma_p^{(v)} \csc(\gamma_p^{(v)} 2h),$$

and

$$\hat{\xi}_p = \frac{1}{d} \int_0^d \xi(x) e^{-i\alpha_p x} dx, \quad \hat{v}_p = \frac{1}{d} \int_0^d v(x) e^{-i\alpha_p x} dx.$$

In the flat-interface, normal incidence case, the data will be  $\xi = -1$  and  $v = (i\gamma^{(u)})$  so that  $\hat{\xi}_p = -1\delta_{p,0}$  and  $\hat{v}_p = (i\gamma^{(u)})\delta_{p,0}$ , and only the specular wavenumber,  $p = 0$ , is excited. Here,  $\delta_{p,q}$  is the Kronecker delta. With this, and multiplying the second and fourth equations by  $-1$ , we find

$$\begin{pmatrix} 1 & -1 & 0 & 0 \\ G_0 & H_0 & K_0 & 0 \\ 0 & 0 & 1 & -1 \\ 0 & K_0 & H_0 & J_0 \end{pmatrix} \begin{pmatrix} a_0 \\ b_0 \\ c_0 \\ d_0 \end{pmatrix} = \begin{pmatrix} \hat{\xi}_0 \\ -\tau^{(u)} \hat{v}_0 \\ 0 \\ 0 \end{pmatrix}.$$

The first and third equations give

$$a_0 = b_0 + \hat{\xi}_0, \quad c_0 = d_0,$$

which simplify the remaining equations to

$$\begin{pmatrix} G_0 + H_0 & K_0 \\ K_0 & H_0 + J_0 \end{pmatrix} \begin{pmatrix} b_0 \\ d_0 \end{pmatrix} = \begin{pmatrix} -G_0 \hat{\xi}_0 - \tau^{(u)} \hat{v}_0 \\ 0 \end{pmatrix}.$$

For future use, we can solve for the Fourier coefficient of the transmitted wave

$$d_0 = \frac{-K_0 \left( -\tau^{(u)} \hat{v}_0 - G_0 \hat{\xi}_0 \right)}{(G_0 + H_0)(H_0 + J_0) - K_0^2}. \quad (5)$$

### B. Doubly Layered Medium

As we demonstrated in [18], for a flat interface configuration at  $z = 0$ , the equations for a doubly layered medium with an interfacial current with non-dimensional conductivity  $\hat{\sigma}^{(g)}$  are

$$u - w + P\tau^{(w)} \partial_z w = \xi, \quad z = 0, \quad (6a)$$

$$\tau^{(u)} \partial_z u - \tau^{(w)} \partial_z w + Sw = \tau^{(u)} v, \quad z = 0, \quad (6b)$$

where

$$S = \begin{cases} ik_0 \hat{\sigma}^{(g)}, & \text{TE,} \\ 0, & \text{TM,} \end{cases} \quad P = \begin{cases} 0, & \text{TE,} \\ \hat{\sigma}^{(g)} / (ik_0), & \text{TM.} \end{cases}$$

Appealing to the (rescaled) Rayleigh expansions

$$u = u(x, z) = \sum_{p=-\infty}^{\infty} \tilde{a}_p e^{i\alpha_p x + i\gamma_p^{(u)} z}, \quad (7a)$$

$$w = w(x, z) = \sum_{p=-\infty}^{\infty} \tilde{d}_p e^{i\alpha_p x - i\gamma_p^{(w)} z}, \quad (7b)$$

cf. Eq. (4), the governing equations, Eq. (6), imply

$$\begin{pmatrix} 1 & -1 + PJ_p \\ -G_p & -J_p + S \end{pmatrix} \begin{pmatrix} \tilde{a}_p \\ \tilde{d}_p \end{pmatrix} = \begin{pmatrix} \hat{\xi}_p \\ \tau^{(u)} \hat{v}_p \end{pmatrix}.$$

As above, we note that only the specular wavenumber,  $p = 0$ , is excited so that the governing equations simplify to

$$\begin{pmatrix} 1 & -1 + PJ_0 \\ -G_0 & -J_0 + S \end{pmatrix} \begin{pmatrix} \tilde{a}_0 \\ \tilde{d}_0 \end{pmatrix} = \begin{pmatrix} \hat{\xi}_0 \\ \tau^{(u)} \hat{v}_0 \end{pmatrix},$$

or, multiplying the second equation by  $-1$ , we have

$$\begin{pmatrix} 1 & -1 + PJ_0 \\ G_0 & J_0 - S \end{pmatrix} \begin{pmatrix} \tilde{a}_0 \\ \tilde{d}_0 \end{pmatrix} = \begin{pmatrix} \hat{\xi}_0 \\ -\tau^{(u)} \hat{v}_0 \end{pmatrix}.$$

From this, we find that the solution for the Fourier coefficient of the transmitted wave is

$$\tilde{d}_0 = \frac{-G_0 \hat{\xi}_0 - \tau^{(u)} \hat{v}_0}{G_0 + J_0 - S - PG_0 J_0}. \quad (8)$$

### 3. EFFECTIVE CURRENT

If the relationship between  $\hat{\sigma}^{(g)}$  and  $\epsilon^{(g)}$  [e.g., Eq. (1) or Eq. (2)] is to be *consistent*, then the  $d_0$  from Eq. (5) must be correctly related to  $\tilde{d}_0$  from Eq. (8). At this point, we specialize the calculations of Section A to that of a sheet of graphene of thickness  $h = d_g/2$  and permittivity  $\epsilon^{(v)} = \epsilon^{(g)}$ . We make our results precise in the fundamental result of this paper.

**Theorem 3.1.** For  $d_0$  from Eq. (5) to be consistent with  $\tilde{d}_0$  from Eq. (8), we must have the relation

$$\hat{\sigma}^{(g)} = \frac{k_0 d_g E(h)}{i}, \quad (9a)$$

where

$$E(h) = \Omega(h) \operatorname{sinc}(\sqrt{\epsilon^{(g)}} k_0 2h) \left( \epsilon^{(g)} + \sqrt{\epsilon^{(u)} \epsilon^{(w)}} \right)$$

$$- B(h) \frac{\left( \sqrt{\epsilon^{(u)} \epsilon^{(w)}} + \epsilon^{(w)} \right)}{2}, \quad (9b)$$

$$B(h) = \frac{\Omega(h) \cos(\sqrt{\epsilon^{(g)}} k_0 2h) - 1}{i\sqrt{\epsilon^{(w)}} k_0 h}, \tag{9c}$$

$$\Omega(h) = \exp(i\gamma^{(w)} h), \tag{9d}$$

and

$$\lim_{h \rightarrow 0} E(h) = E_0 = \epsilon^{(g)} + \frac{\sqrt{\epsilon^{(w)}}}{2} (\sqrt{\epsilon^{(u)}} - \sqrt{\epsilon^{(w)}}).$$

*Proof.* We begin by finding the consistent relationship between  $d_0$  and  $\tilde{d}_0$ . For this, we evaluate  $w$  at  $z = -h$  in Eqs. (4) and (7), respectively:

$$w(x, -h) = \sum_{p=-\infty}^{\infty} d_p e^{i\alpha_p x} e^{-i\gamma_p^{(w)}(-h+h)} = d_0 e^{i\alpha x},$$

$$w(x, -h) = \sum_{p=-\infty}^{\infty} \tilde{d}_p e^{i\alpha_p x} e^{-i\gamma_p^{(w)}(-h)} = \tilde{d}_0 e^{i\alpha x} e^{i\gamma^{(w)} h},$$

so that

$$d_0 = \tilde{d}_0 e^{i\gamma^{(w)} h} = \tilde{d}_0 \Omega.$$

With this, Eqs. (5) and (8) demand that

$$\begin{aligned} \Omega \left( \frac{-G_0 \hat{\xi}_0 - \tau^{(u)} \hat{v}_0}{G_0 + J_0 - S - P G_0 J_0} \right) &= \Omega \tilde{d}_0 \\ &= d_0 = \frac{-K_0 (-\tau^{(u)} \hat{v}_0 - G_0 \hat{\xi}_0)}{(G_0 + H_0)(H_0 + J_0) - K_0^2}, \end{aligned}$$

which demands that

$$\begin{aligned} \Omega \{ (G_0 + H_0)(H_0 + J_0) - K_0^2 \} \\ &= -K_0 \{ G_0 + J_0 - S - P G_0 J_0 \}. \end{aligned}$$

We point out that the *incident data*,  $\{\xi, v\}$ , cancel out in this calculation which does *not* occur if one attempts to reconcile  $a_0$  with  $\tilde{a}_0$ .

Using the fact that

$$\begin{aligned} H_0^2 - K_0^2 &= (\tau^{(g)})^2 (\gamma^{(g)})^2 \{ \cot^2(\gamma^{(g)} 2h) - \csc^2(\gamma^{(g)} 2h) \} \\ &= -(\tau^{(g)})^2 (\gamma^{(g)})^2 \\ &=: -\Gamma^2, \end{aligned}$$

which is *independent* of  $h$ , we have

$$\begin{aligned} \Omega \{ -\Gamma^2 + G_0 J_0 + G_0 H_0 + H_0 J_0 \} \\ &= -K_0 \{ G_0 + J_0 - S - P G_0 J_0 \}. \end{aligned}$$

Solving for the terms involving the current,  $S$  and  $P$ , we find

$$S + G_0 J_0 P = Q + R,$$

where

$$\begin{aligned} Q &:= K_0^{-1} \Omega \{ -\Gamma^2 + G_0 J_0 \}, \\ R &:= (I + K_0^{-1} \Omega H_0)(G_0 + J_0). \end{aligned}$$

We begin our study of these functions by noting the following three facts. First,

$$\begin{aligned} K_0^{-1} &= \frac{1}{-\tau^{(g)} \gamma^{(g)} \csc(\gamma^{(g)} 2h)} \\ &= -\left( \frac{2h}{\tau^{(g)}} \right) \left\{ \frac{\sin(\gamma^{(g)} 2h)}{\gamma^{(g)} 2h} \right\} \\ &= -\left( \frac{2h}{\tau^{(g)}} \right) \text{sinc}(\gamma^{(g)} 2h), \end{aligned}$$

where  $\text{sinc}(z) = \sin(z)/z = \mathcal{O}(1)$  as  $z \rightarrow 0$ . Next,

$$K_0^{-1} H_0 = -\cos(\gamma^{(g)} 2h).$$

Finally, normal incidence ( $\theta = 0$ ) gives  $\alpha = 0$  and

$$\gamma^{(m)} = \sqrt{\epsilon^{(m)}} k_0.$$

We now focus upon  $Q$ :

$$\begin{aligned} Q &= -\left( \frac{2h}{\tau^{(g)}} \right) \text{sinc}(\gamma^{(g)} 2h) \Omega(h) \\ &\quad \times \left( -(\tau^{(g)})^2 (\gamma^{(g)})^2 - \tau^{(u)} \gamma^{(u)} \tau^{(w)} \gamma^{(w)} \right) \\ &= 2h k_0^2 \text{sinc}(\sqrt{\epsilon^{(g)}} k_0 2h) \Omega(h) E_Q, \end{aligned}$$

where

$$E_Q := \tau^{(g)} \epsilon^{(g)} + \frac{\tau^{(u)} \tau^{(w)}}{\tau^{(g)}} \sqrt{\epsilon^{(u)} \epsilon^{(w)}}.$$

Moving to  $R$ , we have

$$\begin{aligned} R &= (\Omega(h) K_0^{-1} H_0 + 1)(G_0 + J_0) \\ &= i\gamma^{(w)} h \left( \frac{-\Omega(h) \cos(\gamma^{(g)} 2h) + 1}{i\gamma^{(w)} h} \right) \\ &\quad \times (\tau^{(u)} (-i\gamma^{(u)}) + \tau^{(w)} (-i\gamma^{(w)})) \\ &= -h k_0^2 B(h) E_R, \end{aligned}$$

where

$$E_R := \tau^{(u)} \sqrt{\epsilon^{(u)} \epsilon^{(w)}} + \tau^{(w)} \epsilon^{(w)}.$$

While  $B$  depends upon  $h$ , it is not difficult to show that  $B$  is  $\mathcal{O}(1)$  as  $h \rightarrow 0$  since

$$\begin{aligned} B(h) &= \frac{\Omega(h) \cos(\gamma^{(g)} 2h) - 1}{i\gamma^{(w)} h} \\ &= \frac{(1 + i\gamma^{(w)} h + \mathcal{O}(h^2))(1 + \mathcal{O}(h^2)) - 1}{i\gamma^{(w)} h} \\ &= \frac{i\sqrt{\epsilon^{(w)}} k_0 h + \mathcal{O}(h^2)}{i\sqrt{\epsilon^{(w)}} k_0 h} \\ &= 1 + \mathcal{O}(h). \end{aligned}$$

So from this, we learn that

$$S + G_0 J_0 P = 2h k_0^2 E(h),$$

where

$$E(h) := \left\{ \Omega(h) \operatorname{sinc} \left( \sqrt{\epsilon^{(g)}} 2h k_0 \right) E_Q - B(h) \frac{E_R}{2} \right\}. \quad (10)$$

We have two polarizations to consider and we note that only  $\{E_Q, E_R\}$  depend upon this. In Transverse Electric (TE), we find

$$E_Q^{\text{TE}} = \epsilon^{(g)} + \sqrt{\epsilon^{(u)} \epsilon^{(w)}}, \quad E_R^{\text{TE}} = \sqrt{\epsilon^{(u)} \epsilon^{(w)}} + \epsilon^{(w)},$$

while in Transverse Magnetic (TM) polarization we have

$$E_Q^{\text{TM}} = 1 + \frac{\epsilon^{(g)}}{\sqrt{\epsilon^{(u)} \epsilon^{(w)}}}, \quad E_R^{\text{TM}} = \frac{\sqrt{\epsilon^{(w)}}}{\sqrt{\epsilon^{(u)}}} + 1.$$

However, straightforward simplification of the previous formulae yields

$$E_Q^{\text{TM}} = \frac{E_Q^{\text{TE}}}{\sqrt{\epsilon^{(u)} \epsilon^{(w)}}}, \quad E_R^{\text{TM}} = \frac{E_R^{\text{TE}}}{\sqrt{\epsilon^{(u)} \epsilon^{(w)}}}.$$

Now, in TE polarization, we have  $P = 0$  so that

$$\hat{\sigma}^{(g)} = \frac{S}{i k_0} = \frac{(2h) k_0}{i} E(h) = \frac{k_0 d_g}{i} E(h), \quad (11)$$

where  $d_g = 2h$ . Meanwhile, in TM polarization, using  $S = 0$ , we find

$$\begin{aligned} \hat{\sigma}^{(g)} &= i k_0 P = \frac{i k_0 \epsilon^{(u)} \epsilon^{(w)}}{\left( -i \sqrt{\epsilon^{(u)}} k_0 \right) \left( -i \sqrt{\epsilon^{(w)}} k_0 \right)} (2h k_0^2) E(h) \\ &= \frac{(2h) k_0}{i} E(h) = \frac{k_0 d_g}{i} E(h), \end{aligned}$$

and we find a single function  $E(h)$  which can be used to define a *consistent* effective current that works for *both* polarizations.

Finally, using the fact that  $\{\Omega(h), B(h), \operatorname{sinc}(\gamma^{(v)} h)\} = \mathcal{O}(1)$  as  $h \rightarrow 0$ , we see that the small-thickness limit of  $\hat{\sigma}^{(g)}$  is

$$\hat{\sigma}_0^{(g)} = \frac{(2h) k_0}{i} E_0 = \frac{k_0 d_g}{i} E_0, \quad (12)$$

where

$$\begin{aligned} E_0 &= \epsilon^{(g)} + \sqrt{\epsilon^{(u)} \epsilon^{(w)}} - \frac{\sqrt{\epsilon^{(u)} \epsilon^{(w)}}}{2} - \frac{\epsilon^{(w)}}{2} \\ &= \epsilon^{(g)} + \frac{\sqrt{\epsilon^{(u)} \epsilon^{(w)}}}{2} - \frac{\epsilon^{(w)}}{2} \\ &= \epsilon^{(g)} + \frac{\sqrt{\epsilon^{(w)}}}{2} \left( \sqrt{\epsilon^{(u)}} - \sqrt{\epsilon^{(w)}} \right). \end{aligned}$$

□

## A. Effective Permittivity of Graphene

Now, we turn to our central purpose: the modeling of graphene. The faithful approximation of the electromagnetic response of

graphene is still a subject of ongoing research [21]. We employ a simple nondimensionalized Drude model which, from [11,22], gives the effective permittivity

$$\epsilon^{(g)} = \frac{i \hat{\sigma}_D}{k_0 d_g} = \left( \frac{i}{k_0 d_g} \right) \left( \frac{\sigma_0}{\epsilon_0 \epsilon_0} \right) \left( \frac{4 E_F}{\pi} \right) \frac{1}{\hbar \gamma - i \hbar \omega}, \quad (13)$$

where  $\hbar$  is the reduced Planck's constant,  $\omega$  is the angular frequency,  $\gamma$  is the relaxation rate, and  $E_F$  is the (local) Fermi level position. We point out that [11,22] asks for an effective current of graphene,

$$\hat{\sigma}^{(g)} = \frac{k_0 d_g \epsilon^{(g)}}{i},$$

cf. Eq. (1), which matches our asymptotic model, Eq. (2), when  $\epsilon^{(u)} = \epsilon^{(w)}$  as  $E_0$  equals  $\epsilon^{(g)}$  in this instance. We now investigate the results of simulations with our bulk simulations of Eq. (3) against the interfacial current model, Eq. (6), with  $\hat{\sigma}^{(g)}$  chosen among the “unmodified” current, Eq. (1); the “asymptotic” model, Eq. (12); and the “full” current, Eq. (11).

## 4. NUMERICAL SIMULATIONS

In this section, we compare the simulation of sheets of *corrugated* graphene by the two approaches we outlined in the Introduction: (i) As a thin layer of small, but *non-zero*, thickness with an effective permittivity  $\epsilon^{(g)}$  from Eq. (13), and (ii) as an interfacial layer of current with effective conductivity  $\hat{\sigma}^{(g)}$  chosen from the “unmodified” current [Eq. (1)], the “asymptotic” model [Eq. (12)], and the “full” current [Eq. (11)].

### A. Numerical Methods

The numerical algorithms we employ for our comparisons have already been described in the literature, more specifically [28,29] for the triply layered configuration and [30,31] in the case of a doubly layered structure with an interfacial current. We now briefly recall each of these and refer the interested reader to the papers listed for complete details.

Regarding the triply layered model, the authors [28,29] describe a high-order spectral approach applied to a transformed field expansion (TFE) restatement of the governing equations, Eq. (3), supplemented with Padé approximation techniques. In summary, a change of variables is effected which maps the *perturbed* geometry  $\{z = h + g(x), z = -h + \ell(x)\}$  to the *trivial* flat-interface one,  $\{z' = h, z' = -h\}$ , resulting in new dependent variables,  $\{\tilde{u}(x', z'), \tilde{v}(x', z'), \tilde{w}(x', z')\}$  which satisfy *inhomogeneous* versions of Eq. (3). Importantly, the inhomogeneities are  $\mathcal{O}(g)$  and  $\mathcal{O}(\ell)$ , which suggests that a boundary perturbation approach, e.g., setting,

$$g(x) = \varepsilon \tilde{g}(x), \quad \ell(x) = \varepsilon \tilde{\ell}(x), \quad \left\{ \tilde{g}, \tilde{\ell} \right\} = \mathcal{O}(1), \quad \varepsilon \ll 1,$$

will be fruitful. We point out that  $\tilde{g}$  and  $\tilde{\ell}$  are dimensionless so that  $\varepsilon$  has the same units as  $g$  and  $\ell$  (e.g., micrometers). Experience has demonstrated the superior performance of the TFE method built upon the expansions

$$\{\tilde{u}, \tilde{v}, \tilde{w}\}(x', z'; \varepsilon) = \sum_{n=0}^{\infty} \{\tilde{u}_n, \tilde{v}_n, \tilde{w}_n\}(x', z') \varepsilon^n,$$

and numerical simulation of the resulting *recursively defined* problems for  $\{\tilde{u}_n, \tilde{v}_n, \tilde{w}_n\}$ . This is accomplished via a Fourier/Legendre Galerkin method based upon forms like

$$\tilde{u}_n(x', z') = \sum_{p=-N_x/2}^{N_x/2-1} \sum_{q=0}^{N_z} \hat{u}_{p,q} e^{i\alpha_p x'} L_q(z'/h),$$

where  $L_q(z)$  is the  $q$ -th Legendre function. Based upon rigorous demonstration [32,33], the smallness assumption on  $\varepsilon$  can be dropped if it is chosen to be *real*. This observation can be realized in numerical simulation with the use of numerical analytical continuation algorithms such as Padé approximation [34] which we use here. This approach we denote the “bulk” simulation of Eq. (3), and we treat it as an exact solution.

Regarding the doubly layered simulations with interfacial graphene, we utilized the scheme of one of the authors [30,31]. Here a somewhat different approach is used where the *volumetric* problem is restated in terms of *interfacial* quantities, namely the surface impedances. For instance, following the approach of Despres [35,36], one defines

$$U(x) := [-\partial_z u + i\eta u]_{z=g(x)}, \quad \tilde{U}(x) := [-\partial_z u - i\eta u]_{z=g(x)},$$

$$W(x) := [\partial_z w - i\eta w]_{z=g(x)}, \quad \tilde{W}(x) := [\partial_z w + i\eta w]_{z=g(x)},$$

for some  $\eta \in \mathbf{R}^+$  and rewrites the boundary conditions at  $z = g(x)$  in Eq. (6) in terms of these, with the understanding that  $\{u, w\}$  satisfy the relevant Helmholtz equations and boundary conditions. At this point, we make the Boundary Perturbation assumption

$$g(x) = \varepsilon \tilde{g}(x), \quad \tilde{g} = \mathcal{O}(1), \quad \varepsilon \ll 1,$$

and expand the impedances in Taylor series

$$\{U, \tilde{U}, W, \tilde{W}\}(x; \varepsilon) = \sum_{n=0}^{\infty} \{U_n, \tilde{U}_n, W_n, \tilde{W}_n\}(x) \varepsilon^n.$$

Insertion of these into the boundary conditions delivers a *recursively defined* sequence of problems (as in the previously shown TFE approach); however, these need only be enforced at the interface,  $z = g(x)$ . The numerical method is a Fourier collocation approach using representations of the form

$$U(x) = \sum_{p=-N_x/2}^{N_x/2-1} \hat{U}_p e^{i\alpha_p x}.$$

As with the TFE method, we avail ourselves of the beneficial properties of numerical analytical continuation via the Padé approximation algorithm [34]. We make three simulations with this approach; the first is “unmodified” [with  $\hat{\sigma}^{(g)}$  given by Eq. (1)], the second is “asymptotic” [with  $\hat{\sigma}^{(g)}$  specified by Eq. (12)], and the third is “full” [with  $\hat{\sigma}^{(g)}$  defined by Eq. (11)].

## B. Numerical Results

In order to assess the performance of our effective conductivities, we study the transmission of our configurations. For this, we recall the Rayleigh expansions, Eq. (7), and the definitions of the efficiencies [27]

$$e_p^{(u)} = \frac{\gamma_p^{(u)}}{\gamma^{(u)}} |\tilde{a}_p|^2, \quad e_p^{(w)} = \frac{\gamma_p^{(w)}}{\gamma^{(w)}} |\tilde{d}_p|^2.$$

From this, we can define the reflection and transmission,

$$R = \sum_{p \in \mathcal{U}} e_p^{(u)}, \quad T = \sum_{p \in \mathcal{W}} e_p^{(w)}, \quad (14)$$

where  $\mathcal{U}$  and  $\mathcal{W}$  are the propagating modes in the upper and lower layers, respectively. As our derivation was based upon matching the transmissions (in the flat-interface case), this is the quantity of interest upon which we focus.

In order to most effectively study the performance of our method, we chose a configuration where the difference between the response of flat-interface and non-flat-interface geometries is maximized. Such an instance can be found at a GSP where a significant enhancement in the scattered field can be found in a small neighborhood of the layer interfaces. In [31] [Fig. 6(b)], we found that a particular double-layer graphene structure generated GSPs at the energies 11 and 26 meV, which we single out for study in the following sections.

## C. Single-Layer Graphene

We began with a configuration featuring a single layer of graphene between two dielectrics (with permittivities  $\epsilon^{(u)}$  and  $\epsilon^{(w)}$ ) mounted on the corrugated interface between the two layers (shaped by  $z = g(x) = \varepsilon \tilde{g}(x)$ ), where

$$\begin{aligned} \epsilon^{(u)} = 1, \quad \epsilon^{(w)} = 11, \quad \tilde{g}(x) = \cos(2\pi x/d), \\ d = 10, \quad 0 \leq \varepsilon \leq 0.4. \end{aligned} \quad (15)$$

We began with low-energy illumination at  $E = 11$  meV (corresponding to  $\lambda \approx 112.7129 \mu\text{m}$ ) and display results of the transmission in Fig. 2 as computed by simulation of the “bulk” three-layer problem, and the two-layer configurations with conductivities specified by the “unmodified,” “asymptotic,” and “full” models specified previously. In addition, in Fig. 3, we show the difference between these latter three and the bulk simulation which we consider exact:

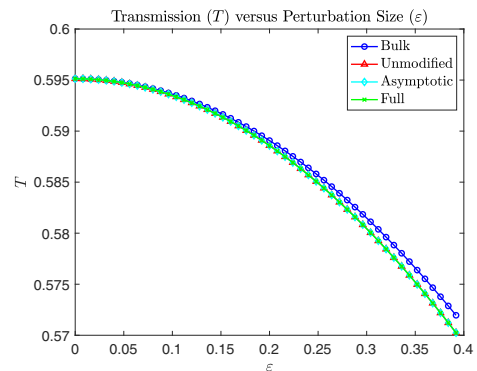


**Fig. 2.** Transmission from a single-sheet graphene configuration, Eq. (15), at  $E = 11$  meV as computed by simulation of the “bulk” three-layer configuration, Eq. (3), and the two-layer structures with interfacial currents which are “unmodified” [with  $\hat{\sigma}^{(g)}$  given by Eq. (1)], “asymptotic” [with  $\hat{\sigma}^{(g)}$  specified by Eq. (12)], and “full” [with  $\hat{\sigma}^{(g)}$  defined by Eq. (11)].

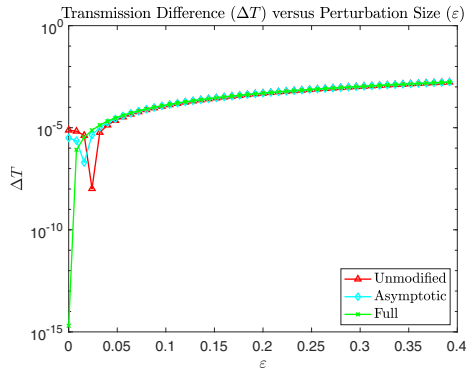


**Fig. 3.** Differences in transmission from a single-sheet graphene configuration, Eq. (15), at  $E = 11$  meV between a simulation of the “bulk” three-layer configuration, Eq. (3), and the two-layer structures with interfacial currents which are “unmodified” [with  $\hat{\sigma}^{(g)}$  given by Eq. (1)], “asymptotic” [with  $\hat{\sigma}^{(g)}$  specified by Eq. (12)], and “full” [with  $\hat{\sigma}^{(g)}$  defined by Eq. (11)].

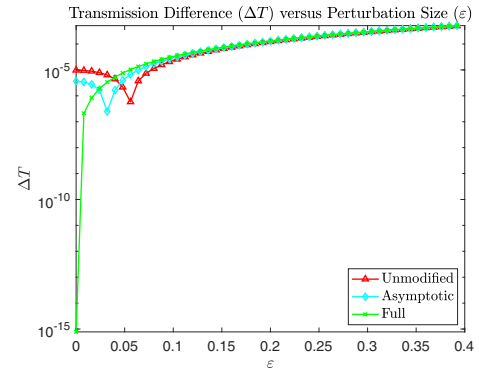


**Fig. 5.** Differences in transmission from a single-sheet graphene configuration, Eq. (15), at  $E = 26$  meV between a simulation of the “bulk” three-layer configuration, Eq. (3), and the two-layer structures with interfacial currents which are “unmodified” [with  $\hat{\sigma}^{(g)}$  given by Eq. (1)], “asymptotic” [with  $\hat{\sigma}^{(g)}$  specified by Eq. (12)], and “full” [with  $\hat{\sigma}^{(g)}$  defined by Eq. (11)].

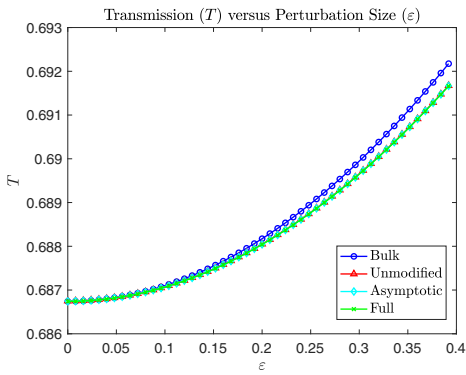


**Fig. 4.** Transmission from a single-sheet graphene configuration, Eq. (15), at  $E = 26$  meV as computed by simulation of the “bulk” three-layer configuration, Eq. (3), and the two-layer structures with interfacial currents which are “unmodified” [with  $\hat{\sigma}^{(g)}$  given by Eq. (1)], “asymptotic” [with  $\hat{\sigma}^{(g)}$  specified by Eq. (12)], and “full” [with  $\hat{\sigma}^{(g)}$  defined by Eq. (11)].

$$\Delta T := |T - T_{\text{bulk}}|.$$

**Remark 4.1.** Here we can clearly see that, while all three models do provide useful (at least moderately accurate) answers, the “full” model that we advocate provides the best results for small values of  $\varepsilon$  ( $0 \leq \varepsilon \leq 0.025$ ) being exact to machine precision when  $\varepsilon = 0$ .

We repeated these experiments for the higher-energy case of illumination at  $E = 26$  meV (corresponding to  $\lambda \approx 47.6862 \mu\text{m}$ ) and show the outcome of our simulations of the transmission in Fig. 4, again for “bulk,” “unmodified,” “asymptotic,” and “full” models of the conductivity. Their differences with the “bulk” simulation are shown in Fig. 5.

**Remark 4.2.** As before, all three models do give reasonable answers, but the “full” model gives the best results for moderate values of  $\varepsilon$  ( $0 \leq \varepsilon \leq 0.04$ ), being exact to machine precision when  $\varepsilon = 0$ .

## D. Double-Layer Graphene

At this point, we decided to test the utility of our new effective conductivity *outside* the scope of our derivation, more specifically as applied to a configuration featuring *two* sheets of graphene. We were also curious what effect the spacing between the graphene sheets had on our results. Therefore, we decided to investigate simulations featuring “small” ( $2 \mu\text{m}$ ), “medium” ( $5 \mu\text{m}$ ), and “large” ( $10 \mu\text{m}$ ) gaps.

To pursue this, we moved to a configuration featuring a double layer of graphene with a gap of width  $2b$  between, mounted in three dielectrics (with permittivities  $\epsilon^{(u)}$ ,  $\epsilon^{(v)}$ , and  $\epsilon^{(w)}$ ) mounted on the corrugated interfaces between the three layers (shaped by  $z = b + g(x) = b + \varepsilon \tilde{g}(x)$  and  $z = -b + \ell(x) = -b + \varepsilon \tilde{\ell}(x)$ ), where

$$\epsilon^{(u)} = 1, \quad \epsilon^{(v)} = 1, \quad \epsilon^{(w)} = 11,$$

$$\tilde{g}(x) = \cos(2\pi x/d), \quad \tilde{\ell}(x) = \cos(2\pi x/d),$$

$$d = 10, \quad 0 \leq \varepsilon \leq 0.1. \quad (16)$$

We began with low-energy illumination at  $E = 11$  meV (corresponding to  $\lambda \approx 112.7129 \mu\text{m}$ ) and display results of the transmission in Figs. 6 ( $2b = 2 \mu\text{m}$ ), 7 ( $2b = 5 \mu\text{m}$ ), and 8 ( $2b = 10 \mu\text{m}$ ) as computed by simulation of the “bulk” five-layer problem, and the three-layer configurations with conductivities specified by the “no modification,” “asymptotic,” and “full” models specified above. In addition, in Figs. 9 ( $2b = 2 \mu\text{m}$ ), 10 ( $2b = 5 \mu\text{m}$ ), and 11 ( $2b = 10 \mu\text{m}$ ), we show the differences between these latter three and the bulk simulation which we consider exact.

**Remark 4.3.** Once again, all three models do give good results, but the “full” model gives the best results for most values of  $\varepsilon$  sampled ( $0 \leq \varepsilon \leq 0.075$ , at least) being exact to machine precision when  $\varepsilon = 0$ .

We concluded with high-energy illumination at  $E = 26$  meV (corresponding to  $\lambda \approx 47.6862 \mu\text{m}$ ) and display results of the transmission in Figs. 12 ( $2b = 2 \mu\text{m}$ ), 13 ( $2b = 5 \mu\text{m}$ ), and 14 ( $2b = 10 \mu\text{m}$ ) as computed by simulation of the “bulk” five-layer problem, and the three-layer

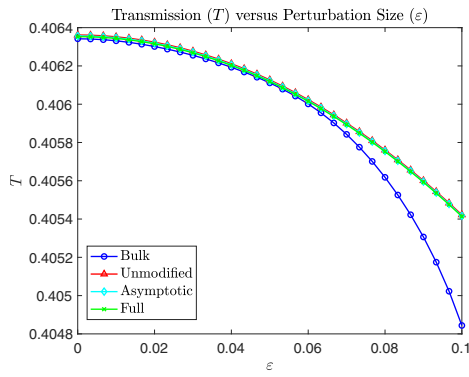


**Fig. 6.** Transmission from a double-sheet graphene configuration, Eq. (16), with  $2b = 2 \mu\text{m}$  at  $E = 11\text{meV}$  as computed by simulation of the “bulk” five-layer configuration and the three-layer structures with interfacial currents which are “unmodified” [with  $\hat{\sigma}^{(\mathcal{G})}$  given by Eq. (1)], “asymptotic” [with  $\hat{\sigma}^{(\mathcal{G})}$  specified by Eq. (12)], and “full” [with  $\hat{\sigma}^{(\mathcal{G})}$  defined by Eq. (11)].

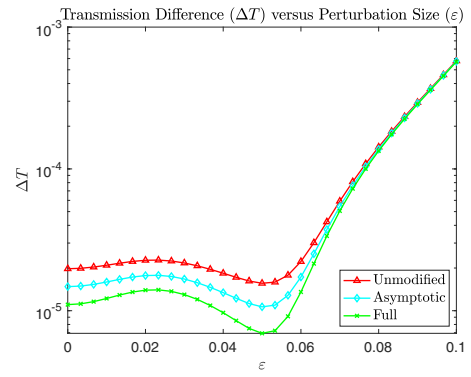


**Fig. 9.** Differences in transmission from a double-sheet graphene configuration, Eq. (16), with  $2b = 2 \mu\text{m}$  at  $E = 11 \text{meV}$  between a simulation of the “bulk” five-layer configuration and the three-layer structures with interfacial currents which are “unmodified” [with  $\hat{\sigma}^{(\mathcal{G})}$  given by Eq. (1)], “asymptotic” [with  $\hat{\sigma}^{(\mathcal{G})}$  specified by Eq. (12)], and “full” [with  $\hat{\sigma}^{(\mathcal{G})}$  defined by Eq. (11)].

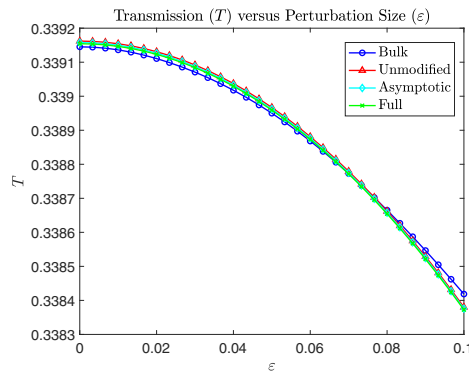


**Fig. 7.** Transmission from a double-sheet graphene configuration, Eq. (16), with  $2b = 5 \mu\text{m}$  at  $E = 11 \text{meV}$  as computed by simulation of the “bulk” five-layer configuration and the three-layer structures with interfacial currents which are “unmodified” [with  $\hat{\sigma}^{(\mathcal{G})}$  given by Eq. (1)], “asymptotic” [with  $\hat{\sigma}^{(\mathcal{G})}$  specified by Eq. (12)], and “full” [with  $\hat{\sigma}^{(\mathcal{G})}$  defined by Eq. (11)].

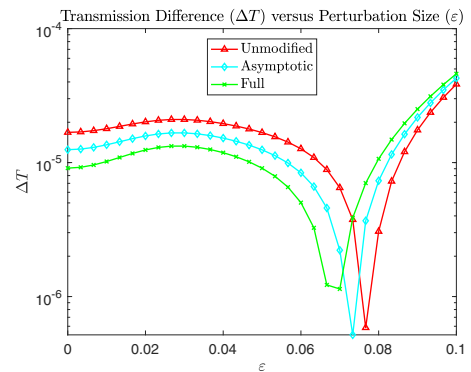


**Fig. 10.** Differences in transmission from a double-sheet graphene configuration, Eq. (16), with  $2b = 5 \mu\text{m}$  at  $E = 11 \text{meV}$  between a simulation of the “bulk” five-layer configuration and the three-layer structures with interfacial currents which are “unmodified” [with  $\hat{\sigma}^{(\mathcal{G})}$  given by Eq. (1)], “asymptotic” [with  $\hat{\sigma}^{(\mathcal{G})}$  specified by Eq. (12)], and “full” [with  $\hat{\sigma}^{(\mathcal{G})}$  defined by Eq. (11)].

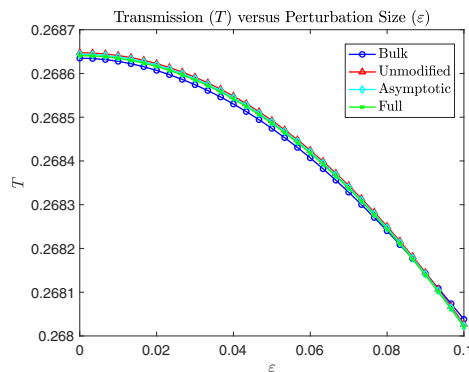


**Fig. 8.** Transmission from a double-sheet graphene configuration, Eq. (16), with  $2b = 10 \mu\text{m}$  at  $E = 11 \text{meV}$  as computed by simulation of the “bulk” five-layer configuration and the three-layer structures with interfacial currents which are “unmodified” [with  $\hat{\sigma}^{(\mathcal{G})}$  given by Eq. (1)], “asymptotic” [with  $\hat{\sigma}^{(\mathcal{G})}$  specified by Eq. (12)], and “full” [with  $\hat{\sigma}^{(\mathcal{G})}$  defined by Eq. (11)].

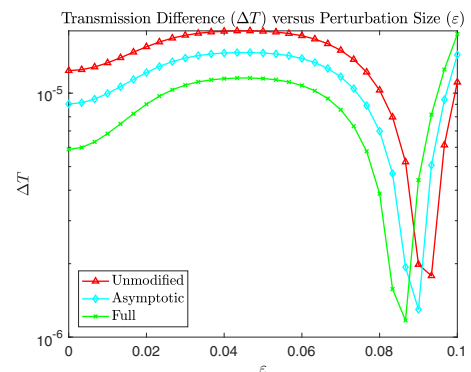


**Fig. 11.** Differences in transmission from a double-sheet graphene configuration, Eq. (16), with  $2b = 10 \mu\text{m}$  at  $E = 11 \text{meV}$  between a simulation of the “bulk” five-layer configuration and the three-layer structures with interfacial currents which are “unmodified” [with  $\hat{\sigma}^{(\mathcal{G})}$  given by Eq. (1)], “asymptotic” [with  $\hat{\sigma}^{(\mathcal{G})}$  specified by Eq. (12)], and “full” [with  $\hat{\sigma}^{(\mathcal{G})}$  defined by Eq. (11)].

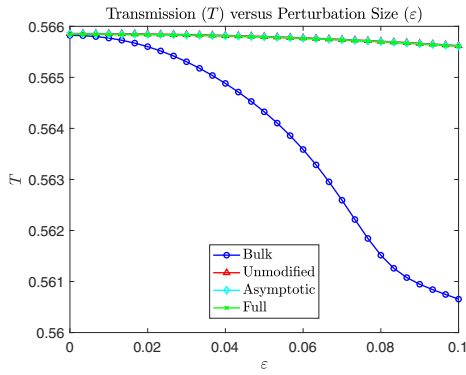


**Fig. 12.** Transmission from a double-sheet graphene configuration, Eq. (16), with  $2h = 2 \mu\text{m}$  at  $E = 26 \text{ meV}$  as computed by simulation of the “bulk” five-layer configuration and the three-layer structures with interfacial currents which are “unmodified” [with  $\hat{\sigma}^{(\mathcal{G})}$  given by Eq. (1)], “asymptotic” [with  $\hat{\sigma}^{(\mathcal{G})}$  specified by Eq. (12)], and “full” [with  $\hat{\sigma}^{(\mathcal{G})}$  defined by Eq. (11)].

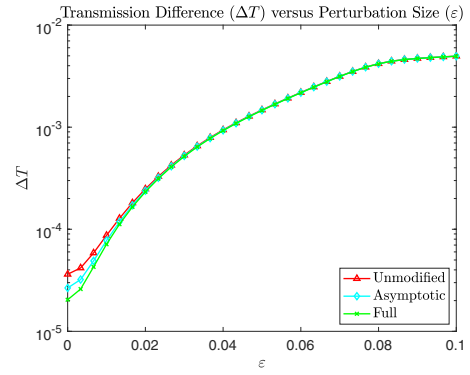


**Fig. 15.** Differences in transmission from a double-sheet graphene configuration, Eq. (16), with  $2h = 2 \mu\text{m}$  at  $E = 26 \text{ meV}$  between a simulation of the “bulk” five-layer configuration and the three-layer structures with interfacial currents which are “unmodified” [with  $\hat{\sigma}^{(\mathcal{G})}$  given by Eq. (1)], “asymptotic” [with  $\hat{\sigma}^{(\mathcal{G})}$  specified by Eq. (12)], and “full” [with  $\hat{\sigma}^{(\mathcal{G})}$  defined by Eq. (11)].

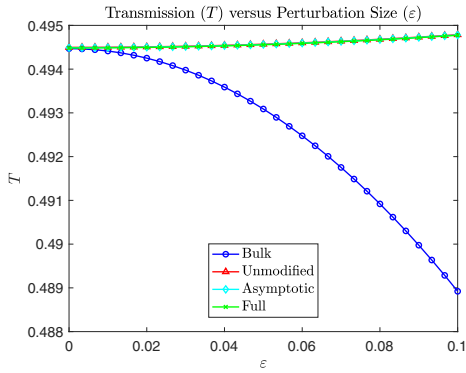


**Fig. 13.** Transmission from a double-sheet graphene configuration, Eq. (16), with  $2h = 5 \mu\text{m}$  at  $E = 26 \text{ meV}$  as computed by simulation of the “bulk” five-layer configuration and the three-layer structures with interfacial currents which are “unmodified” [with  $\hat{\sigma}^{(\mathcal{G})}$  given by Eq. (1)], “asymptotic” [with  $\hat{\sigma}^{(\mathcal{G})}$  specified by Eq. (12)], and “full” [with  $\hat{\sigma}^{(\mathcal{G})}$  defined by Eq. (11)].

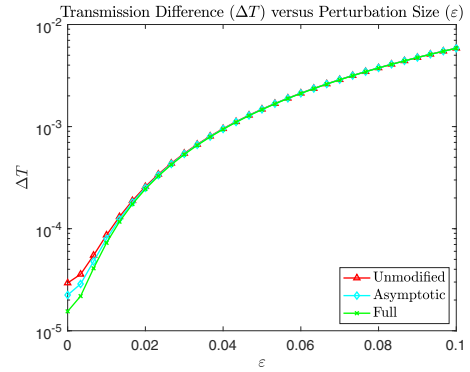


**Fig. 16.** Differences in transmission from a double-sheet graphene configuration, Eq. (16), with  $2h = 5 \mu\text{m}$  at  $E = 26 \text{ meV}$  between a simulation of the “bulk” five-layer configuration and the three-layer structures with interfacial currents which are “unmodified” [with  $\hat{\sigma}^{(\mathcal{G})}$  given by Eq. (1)], “asymptotic” [with  $\hat{\sigma}^{(\mathcal{G})}$  specified by Eq. (12)], and “full” [with  $\hat{\sigma}^{(\mathcal{G})}$  defined by Eq. (11)].

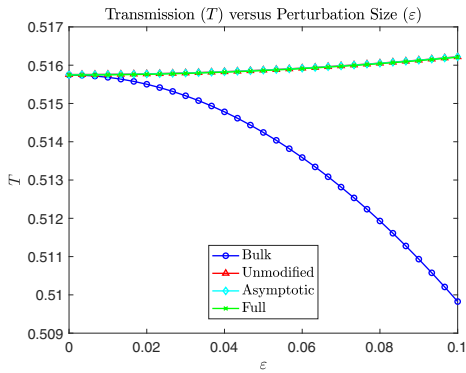


**Fig. 14.** Transmission from a double-sheet graphene configuration, Eq. (16), with  $2h = 10 \mu\text{m}$  at  $E = 26 \text{ meV}$  as computed by simulation of the “bulk” five-layer configuration and the three-layer structures with interfacial currents which are “unmodified” [with  $\hat{\sigma}^{(\mathcal{G})}$  given by Eq. (1)], “asymptotic” [with  $\hat{\sigma}^{(\mathcal{G})}$  specified by Eq. (12)], and “full” [with  $\hat{\sigma}^{(\mathcal{G})}$  defined by Eq. (11)].

configurations with conductivities specified by the “no modification,” “asymptotic,” and “full” models specified previously. In addition, in Figs. 15 ( $2h = 2 \mu\text{m}$ ), 16 ( $2h = 5 \mu\text{m}$ ), and 17 ( $2h = 10 \mu\text{m}$ ), we show the differences between these latter three and the bulk simulation, which we consider exact.

**Remark 4.4.** Again, all three models do give passable answers, but the “full” model gives the best results for all values of  $\epsilon$  sampled, again being exact to machine precision when  $\epsilon = 0$ .

**E. Summary**

There are crucial conclusions to draw from these results. In Figs. 3 and 5, we see that the “full” model is most accurate, and the “asymptotic” model second, on the ranges  $0 \leq \epsilon \leq 0.025$  and  $0 \leq \epsilon \leq 0.04$ , respectively. Interestingly, Figs. 9, 10, and 11 reveal the same relative performance of the models on the much larger range  $0 \leq \epsilon \leq 0.075$ . Finally, from Figs. 15–17, we learn that the same ordering holds over the entire range of  $\epsilon$  that we studied. From this, we conclude that the “full” model we

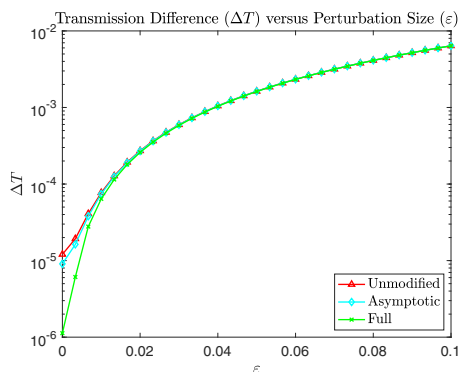


**Fig. 17.** Differences in transmission from a double-sheet graphene configuration, Eq. (16), with  $2b = 10 \mu\text{m}$  at  $E = 26 \text{ meV}$  between a simulation of the “bulk” five-layer configuration and the three-layer structures with interfacial currents which are “unmodified” [with  $\hat{\sigma}^{(g)}$  given by Eq. (1)], “asymptotic” [with  $\hat{\sigma}^{(g)}$  specified by Eq. (12)], and “full” [with  $\hat{\sigma}^{(g)}$  defined by Eq. (11)].

describe is always more accurate for  $\varepsilon$  sufficiently small, and in some cases the range of  $\varepsilon$  can be quite large.

**Funding.** National Science Foundation (DMS-1813033); Simons Foundation; National Research Foundation of Korea (NRF-2021R1A2C1093579).

**Acknowledgment.** D. P. N. gratefully acknowledges support from the NSF. Y. H. gratefully acknowledges support from a Collaboration Grant for Mathematicians, Simons Foundation, and National Research Foundation of Korea (NRF) funded by the Ministry of Education (NRF-2021R1A2C1093579).

**Disclosures.** The authors declare no conflicts of interest.

**Data Availability.** Data underlying the results presented in this paper are not publicly available at this time but may be obtained from the authors upon reasonable request.

## REFERENCES

1. F. Bonaccorso, Z. Sun, T. Hasan, and A. C. Ferrari, “Graphene photonics and optoelectronics,” *Nat. Photonics* **4**, 611–622 (2010).
2. A. Geim, “Random walk to graphene (Nobel lecture),” *Angew. Chem. (Int. Ed.)* **50**, 6966–6985 (2011).
3. K. Novoselov, “Graphene: materials in the flatland (Nobel lecture),” *Angew. Chem. (Int. Ed.)* **50**, 6986–7002 (2011).
4. A. N. Grigorenko, M. Polini, and K. S. Novoselov, “Graphene plasmonics,” *Nat. Photonics* **6**, 749–758 (2012).
5. T. Low, A. Chaves, J. Caldwell, A. Kumar, N. Fang, P. Avouris, T. Heinz, F. Guinea, L. Martin-Moreno, and F. Koppens, “Polaritons in layered two-dimensional materials,” *Nat. Mater.* **16**, 182–194 (2017).
6. D. N. Basov, M. M. Fogler, and F. J. Garcia de Abajo, “Polaritons in Van der Waals materials,” *Science* **354**, aag1992 (2016).
7. D. Alcaraz Iranzo, S. Nanot, E. J. C. Dias, I. Epstein, C. Peng, D. K. Efetov, M. B. Lundberg, R. Parret, J. Osmond, J.-Y. Hong, J. Kong, D. R. Englund, N. M. R. Peres, and F. H. L. Koppens, “Probing the ultimate plasmon confinement limits with a Van der Waals heterostructure,” *Science* **360**, 291–295 (2018).
8. I.-H. Lee, D. Yoo, P. Avouris, T. Low, and S.-H. Oh, “Graphene acoustic plasmon resonator for ultrasensitive infrared spectroscopy,” *Nat. Nanotechnol.* **14**, 313–319 (2019).
9. M. Jablan, H. Buljan, and M. Soljačić, “Plasmonics in graphene at infrared frequencies,” *Phys. Rev. B* **80**, 245435 (2009).
10. F. H. L. Koppens, D. E. Chang, and F. J. Garcia de Abajo, “Graphene plasmonics: a platform for strong light-matter interactions,” *Nano Lett.* **11**, 3370–3377 (2011).

11. A. Audatore, C. de Angelis, A. Locatelli, and A. B. Aceves, “Tuning of surface plasmon polaritons beat length in graphene directional couplers,” *Opt. Lett.* **38**, 4228–4231 (2013).
12. F. J. Garcia de Abajo, “Graphene plasmonics: challenges and opportunities,” *ACS Photon.* **1**, 135–152 (2014).
13. T. Low and P. Avouris, “Graphene plasmonics for terahertz to mid-infrared applications,” *ACS Nano* **8**, 1086 (2014).
14. COMSOL, *COMSOL Multiphysics Reference Manual* (COMSOL, 2019).
15. I.-H. Lee, M. He, X. Zhang, Y. Luo, S. Liu, J. H. Edgar, K. Wang, P. Avouris, T. Low, J. D. Caldwell, and S.-H. Oh, “Image polaritons in boron nitride for extreme polariton confinement with low losses,” *Nat. Commun.* **11**, 3649 (2020).
16. B. Gallinet, J. Butet, and O. J. F. Martin, “Numerical methods for nanophotonics: standard problems and future challenges,” *Laser Photon. Rev.* **9**, 577–603 (2015).
17. D. P. Nicholls, “Three-dimensional acoustic scattering by layered media: a novel surface formulation with operator expansions implementation,” *Proc. R. Soc. London A* **468**, 731–758 (2012).
18. D. P. Nicholls, “Numerical simulation of grating structures incorporating two-dimensional materials: a high-order perturbation of surfaces framework,” *SIAM J. Appl. Math.* **78**, 19–44 (2018).
19. D. P. Nicholls, “High-order spectral simulation of graphene ribbons,” *Commun. Comput. Phys.* **26**, 1575–1596 (2019).
20. Y. Bludov, A. Ferreira, N. Peres, and M. Vasilievskiy, “A primer on surface plasmon-polaritons in graphene,” *Int. J. Mod. Phys. B* **27**, 1341001 (2013).
21. P. A. D. Goncalves and N. M. R. Peres, *An Introduction to Graphene Plasmonics* (World Scientific, 2016).
22. C. D. Angelis, A. Locatelli, A. Mutti, and A. Aceves, “Coupling dynamics of 1D surface plasmon polaritons in hybrid graphene systems,” *Opt. Lett.* **41**, 480–483 (2016).
23. M. Maier, D. Margetis, and M. Luskun, “Dipole excitation of surface plasmon on a conducting sheet: finite element approximation and validation,” *J. Comput. Phys.* **339**, 126–145 (2017).
24. M. Maier, D. Margetis, and M. Luskun, “Generation of surface plasmon-polaritons by edge effects,” *Commun. Math. Sci.* **16**, 77–95 (2018).
25. J. H. Song, M. Maier, and M. Luskun, “Adaptive finite element simulations of waveguide configurations involving parallel 2D material sheets,” *Comput. Methods Appl. Mech. Eng.* **351**, 20–34 (2019).
26. D. P. Nicholls and S.-H. Oh, “Launching graphene surface plasmon waves with vanishingly small periodic grating structures,” *J. Opt. Soc. Am. A* **38**, 556–563 (2021).
27. R. Petit, ed., *Electromagnetic Theory of Gratings* (Springer-Verlag, 1980).
28. Y. Hong and D. P. Nicholls, “A stable high-order perturbation of surfaces method for numerical simulation of diffraction problems in triply layered media,” *J. Comput. Phys.* **330**, 1043–1068 (2017).
29. Y. Hong and D. P. Nicholls, “A high-order perturbation of surfaces method for scattering of linear waves by periodic multiply layered gratings in two and three dimensions,” *J. Comput. Phys.* **345**, 162–188 (2017).
30. D. P. Nicholls, “Stable, high-order computation of impedance-impedance operators for three-dimensional layered media simulations,” *Proc. R. Soc. London A* **474**, 20170704 (2018).
31. D. P. Nicholls, “On analyticity of scattered fields in layered structures with interfacial graphene,” *Stud. Appl. Math.* **147**, 527–576 (2021).
32. D. P. Nicholls and F. Reitich, “Analytic continuation of Dirichlet-Neumann operators,” *Numer. Math.* **94**, 107–146 (2003).
33. D. P. Nicholls and M. Taber, “Joint analyticity and analytic continuation for Dirichlet-Neumann operators on doubly perturbed domains,” *J. Math. Fluid Mech.* **10**, 238–271 (2008).
34. G. A. Baker, Jr. and P. Graves-Morris, *Padé Approximants*, 2nd ed. (Cambridge University, 1996).
35. B. Després, “Méthodes de décomposition de domaine pour les problèmes de propagation d’ondes en régime harmonique. Le théorème de Borg pour l’équation de Hill vectorielle,” thèse (Institut National de Recherche en Informatique et en Automatique (INRIA)/Université de Paris IX, 1991).
36. B. Després, “Domain decomposition method and the Helmholtz problem,” *Mathematical and Numerical Aspects of Wave Propagation Phenomena*, Strasbourg, France, SIAM, 1991, pp. 44–52.